Supplementary Information

Boosting Aqueous Non-Flow Zinc-Bromine Batteries with a Two-Dimensional Metal-Organic Framework Host: An Adsorption-Catalysis Approach

Hua Wei,[a,b,c] Guangmeng Qu,[c] Xiangyong Zhang,[a,c] Baohui Ren,[a,c] Shizhen Li,[a,c] Jingjing Jiang, [a,c] Yihan Yang,[c] Jinlong Yang,[a] Lingzhi Zhao,[d] Hongfei Li,[e*] Chunyi Zhi[c,f*] and Zhuoxin Liu[a*]

[a]College of Materials Science and Engineering, Shenzhen University, Shenzhen 518055, China

[b]College of Physics and Optoelectronic Engineering, Shenzhen University, Shenzhen 518060, China

[c]Songshan Lake Materials Laboratory, Dongguan, Guangdong 523808, China

[d]Guangdong Provincial Engineering Technology Research Center for Low Carbon and Advanced Energy Materials, Institute of Semiconductor Science and Technology, South China Normal University, Guangzhou 510631, China

[e]School of System Design and Intelligent Manufacturing, Southern University of Science and Technology, Shenzhen 518055, China

[f]Department of Materials Science and Engineering, City University of Hong Kong, 83 Tat Chee Avenue, Kowloon, Hong Kong 999077, China

*Corresponding authors

Email: lihf@sustech.edu.cn; cy.zhi@cityu.edu.hk; liuzhuoxin@szu.edu.cn

Experimental Section

Synthesis of NiPPc and PPc

Pyromellitic dianhydride (PDA, 1.26 g, Macklin, AR), $NiCl_2$ (0.39 g, Aladdin, 99.7%), urea (2.46 g, Macklin, AR), NH_4Cl (0.60 g, Macklin, GR) and $(NH_4)_2Mo_2O_7$ (0.015 g, Macklin, 56.5%) were ground together in solid and then transferred to a muffle roaster. The mixture was heated at 220 ◦C for 3 h. Finally, the acquired solid was then thoroughly washed with water, acetone, and methanol to remove redundant impurities. The as-obtained product was dried in oven under vacuum at 60 ◦C overnight to get NiPPc. Polyphthalocyanine (PPc) was synthesized in a similar procedure without the use of $NiCl_2$.[1]

Preparation of working electrodes in BrRR and BrOR

The catalyst suspension was prepared by dispersing 1.5 mg of catalyst, 1.5 mg of Ketjen Black, and 80 μL of Nafion solution (5 wt.%) into a mixed solution of 1 mL of water-ethanol (volume ratio of 4:1) and sonicating for 30 mins. Afterwards, 5 μL of the ink was dropped onto the working electrode (glassy carbon electrode (GCE), 3 mm diameter).

Fabrication of cathodes in coin cells

NiPPc or PPC powders, KBr (Aladdin), carbon conductor (Ketjen Black), and polyvinylidene fluoride (Aladdin) binder were dispersed into N-methyl pyrrolidone solvent with a mass ratio of 3:3:3:1. The slurry was vigorously stirred for 5 hours, and subsequently coated onto the hydrophobic carbon cloth surface. The coated material was then dried at 60 ºC for 24 hours under vacuum conditions. The mass loading of KBr in cathodes for electrochemical measurement was controlled to ~1 mg cm^{-2}.

Preparation of Br_3^- standard solution

The solution that contains Br_3^- was prepared through a previously reported method[2] and could be described as follows:

$$NaBrO_3 + 5Br^- + 6H^+ \rightarrow 3Br_2\,(aq) + 3H_2O$$

$$Br_2\,(aq) + Br^- \rightleftharpoons Br_3^-\ (K_{eq}=16.1\ M^{-1})$$

Typically, 5 ml of 2 M HBr, 5 ml of 2 M KBr, and 10 ml of 0.1 M $NaBrO_3$ were combined in a glass vial and stirred for 10 min to prepare 20 ml of solution that contains 120 mM Br_3^-, which shows dark orange.

Materials characterizations

X-ray diffraction (XRD) patterns were obtained using a Rigaku Mini Flex 600 system with Cu Kα radiation (λ = 0.154 nm) in the range of 10° to 80°. The morphology and structure of active materials were investigated using a JEM F200 transmission electron microscope. X-ray photoelectron spectroscopy (XPS) measurements was conducted on a Thermo Fisher ESCALAB 250Xi equipped with a monochromatic Al Kα source (1486.6 eV) to confirm the chemical state of each element. Raman spectroscopy and transmission FTIR spectra were collected using a Horiba LabRam HR Evolution spectrometer and an INVENIO-R spectrometer, respectively. The in-situ observation of the optical microscopy images of charge/discharge processes of NiPPc-KBr electrode were carried out in a transparent cuboid electrolytic cell recording by industrial microscope (KYH3800S42, KangYuan Electronic). The extended X-ray absorption fine structure (EXAFS) spectroscopy were collected at BL14A2 beamline of SPring 8.

Electrochemical measurements

The BrRR and BrOR electrochemical measurements of the as-prepared working electrodes were studied with a standard three-electrode system using a CHI 660E electrochemical workstation at room temperature. The standard three-electrode system was adopted with a Hg/Hg_2Cl_2 electrode (SCE, KCl-saturated) and a platinum electrode as the reference electrode and the counter electrode, respectively, and the glassy carbon electrode modified with catalysts as the working electrode. All the reported potentials in this work were referenced to a reversible hydrogen electrode (RHE) based on the equation (Evs. RHE = Evs. SCE + 0.241 + 0.059 pH). The linear sweep voltammetry (LSV) was conducted at a scan rate of 2 mV s^{-1}.

The electrochemical tests of Zn||KBr-NiPPc full battery were carried out by assembling CR2032 coin-type cells at room temperature, employing 0.1 mm Zn foil as the anode and 100 μL 2 M $Zn(SO_4)_2$ (Aladdin) as the aqueous electrolyte. Electrochemical performance (including cyclic performance, rate performance discharge-discharge curves, and electrochemical impedance spectroscopy) was measured on a LAND CT2001A battery test station and a CHI 760D electrochemical workstation.

Computational details

All calculations were performed based on density functional theory (DFT) for first-principles simulations.[3,4] The calculations of adsorption energy, Bader charge, PDOS, etc., were all performed using the Vienna Ab initio Simulation Pack-age (VASP) with the Perdew-Burke-Ernzerhof (PBE) exchange-correlation functional and the projector-augmented-wave (PAW) approach.[5,6] The plane-wave cutoff energy was set to 450eV.

For structure optimization and electronic structure calculation, the (001) surface of NiPPc was used for the calculation according to the XRD results where a pronounced (001) peak was observed, and the Brillouin zone was sampled in k-space using a Monkhorst-Pack scheme of 1×1×1 considering both computational accuracy and efficiency. The convergence criteria of all computational simulations were set as 10^{-5} eV in energy and 0.02 eV $Å^{-1}$ in force. The differential charge density map was obtained using the VASPKIT program and the VESTA software.[7]

The surface electrostatic potential of the material was calculated using DMol3 program in Material Studio 2019 (MS) from Accelrys.[8,9] The global orbital cutoff was set at 3.5 Å. Using the modeling function of VESTA, the model of NiPPc was established by selecting the P4/mmm and I4/mmm space groups. The XRD card was exported in the Power Diffraction Pattern options.

The Gibbs free energy change (ΔG) of each elementary step was calculated by the following equation:

$$\Delta G = \Delta E + \Delta E_{ZPE} - T\Delta S \quad (1)$$

where T is the temperature set at 298.15 K, ΔE is the DFT energy, ΔE_{ZPE} is the zero point energy, and ΔS is the entropy value. The zero point energy and free energy corrections weree both implemented through the VASPKIT program.

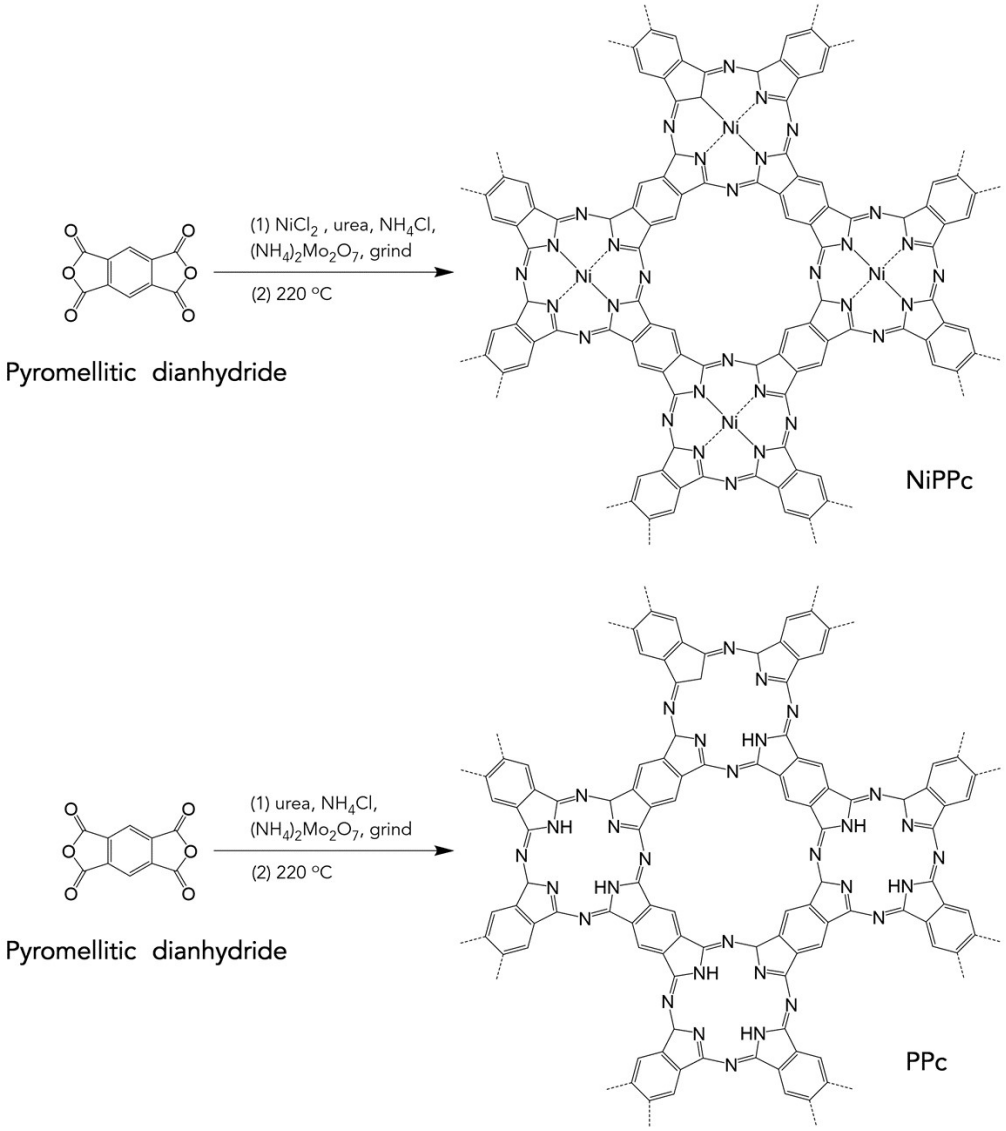

Figure S1. Synthesis route of NiPPc and PPc.[1]

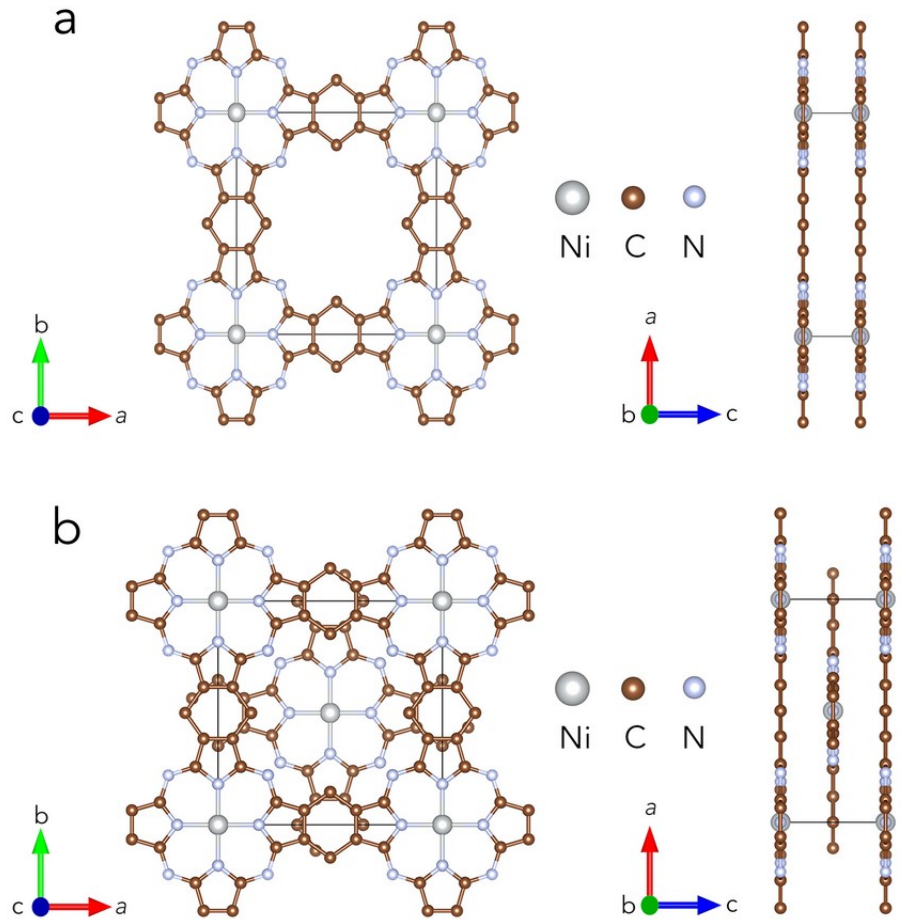

Figure S2. The unit-cell structures of NiPPc derived using the (a) AA stacking and (b) AB stacking models.

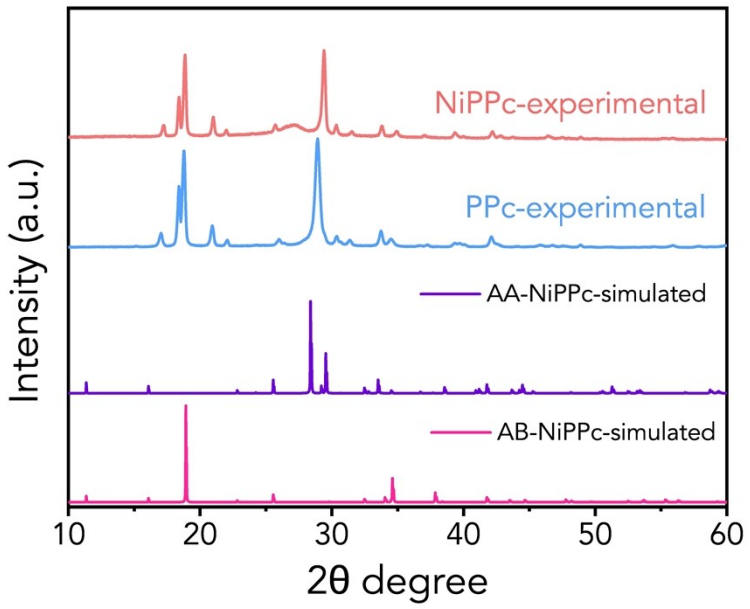

Figure S3. XRD patterns of NiPPc, PPc, and AA stacking-NiPPc and AB stacking-NiPPc simulated by VESTA.

To validate the successful synthesis of NiPPc, we utilized VESTA software to manually input the atomic positions and exported the corresponding PDF cards using the Power Diffraction Pattern options.

we constructed two π–π stacked crystal structures, *i.e.*, AA and AB stacking structures. As demonstrated in Figure S2, the AB stacking structure exhibits distinct characteristics from most two-dimensional covalent organic frameworks with AA stacking models. The AB stacking models generally display lower energy levels, resulting in greater stability compared to AA stacking structures. The stronger interactions between adjacent layers in the AB stacking model leads to a more densely packed and stable structure. Moreover, the AB stacking model offers more space to accommodate molecules or ions, rendering it more suitable for specific applications. We present in Figure S3 the XRD patterns of NiPPc, PPc, AA stacking-NiPPc, and AB stacking-NiPPc simulated by VESTA. Notably, the NiPPc sample matches the XRD patterns of the standard cards simulated by VESTA, indicating the successful synthesis of the polyphthalocyanine framework.

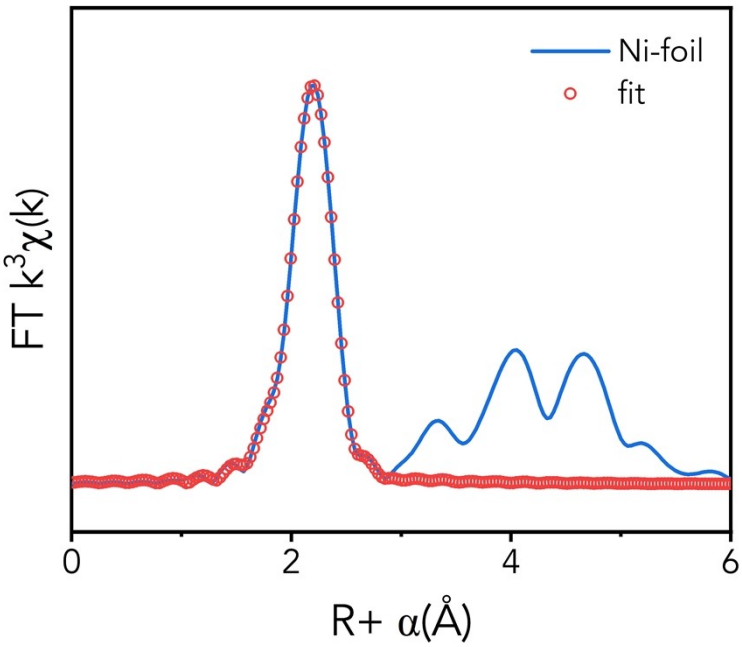

Figure S4. The EXAFS fitting curve of Ni-foil.

The Fourier transformed fitting was carried out in Artemis (version 0.9.26). The k^3 weighting, k-range of 3 – ~15.5 $Å^{-1}$, and R range of 1 – 3 Å were used for the fitting of Ni foil; The k^3 weighting, k-range of 3 – ~11.5 $Å^{-1}$, and R range of 1 – 2 Å were used for the fitting of sample. The four parameters, Niordination number, bond length, Debye-Waller factor, and E_0 shift (CN, R, ΔE_0) were fitted without anyone was fixed, the σ^2 was set.

For Wavelet Transform analysis, the χ(k) exported from Athena was imported into the Hama Fortran Nide. The parameters were listed as follow: R range, 0 – 4 Å, k range, 0 – 14 $Å^{-1}$ for samples; k weight, 2; Morlet function with $\kappa = 10$, $\sigma = 1$ was used as the mother wavelet to provide the overall distribution.

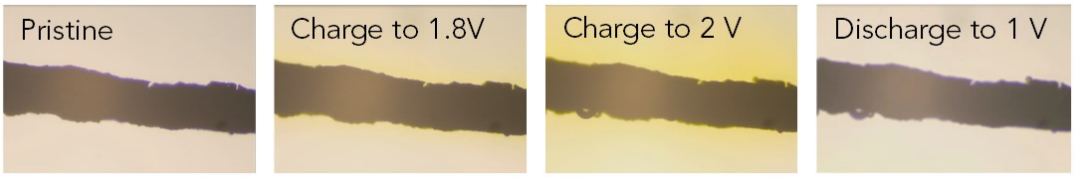

Figure S5. Optical micrographs extracted from the charge/discharge processes of NiPPc-KBr electrodes.

The NiPPc-KBr slurry was coated onto a 0.1 mm platinum wire as the positive electrode, a 1 mm zinc wire was employed as the negative electrode, and 2 M $ZnSO_4$ was used as the electrolyte. When charged from 1 V to 1.8 V, the formation of orange bromine/polybromides was observed. As the charging continued to 2 V, a richer and thicker orange color appeared around the electrode, indicating the significant generation of bromine/polybromides. When discharged to 1 V, the electrolyte color reverted to the pristine state, demonstrating good reversibility of the reaction.

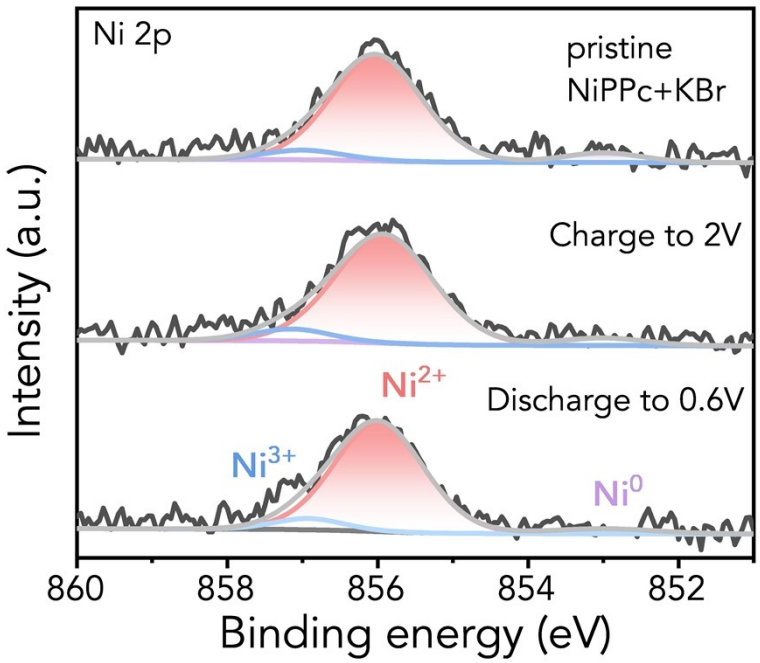

Figure S6. Ni 2p XPS spectra of KBr-NiPPc at specific voltages during the charge/discharge processes.

To understand the surface electronic structure of Ni, the high-resolution XPS of Ni 2p spectra during the charge-discharge process of Zn||KBr-NiPPc was analyzed. In general, the peak of Ni 2p3/2 can be deconvoluted into three peaks centered at around 852.8, 854.9, and 856.2 eV, corresponding to Ni^0, Ni^{2+}, and Ni^{3+}, respectively.[10, 11] While in the nickel phthalocyanine structure, the Ni 2p peak appears at ~855.9 eV due to Ni–N bonds.[12] As shown in Figure S6, for the pristine KBr-NiPPc, a broad single peak was identified at 855.9 eV, corresponding to the Ni in Ni–N_4 site. When charged to 2 V and discharged to 0.6 V, the peak shape and position of the Ni 2p remained unchanged.

Therefore, it can be inferred that throughout the charge-discharge processes, nickel within the Ni–N_4 sites remained stable, without any changes to its oxidation state.

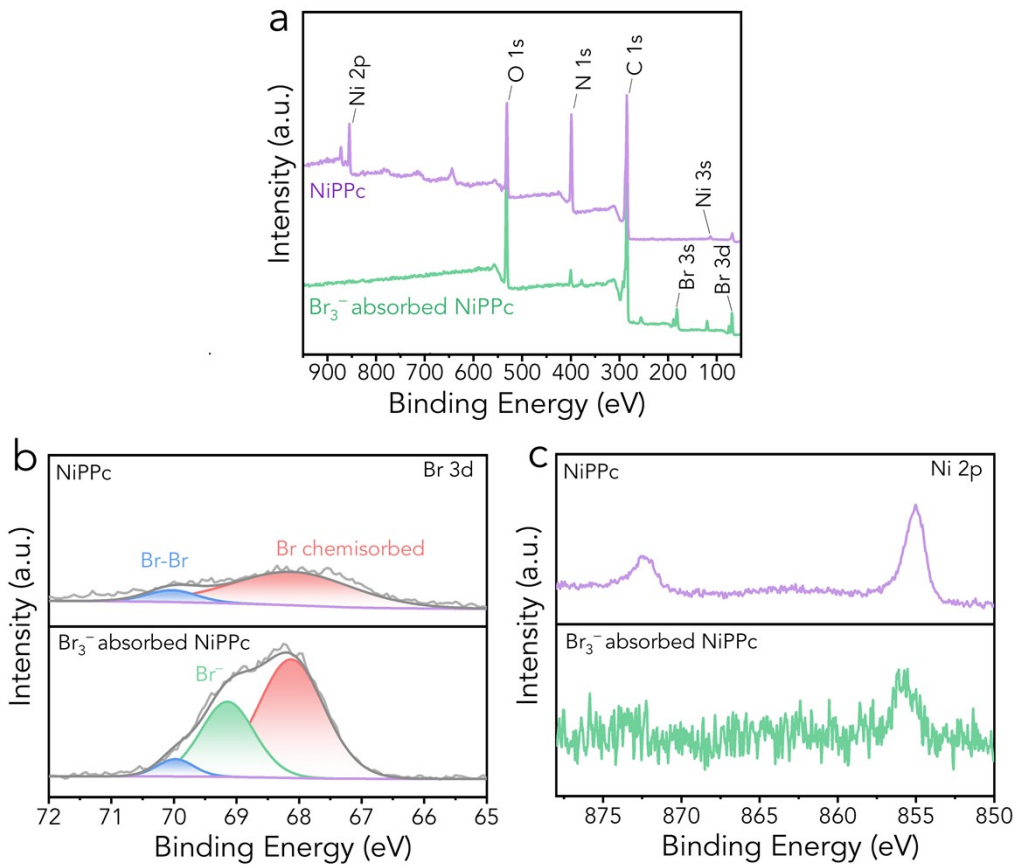

Figure S7. XPS spectra of (a) survey, (b) Br 3d, and (c) Ni 2p for the NiPPc and the Br_3^- absorbed sample.

Figure S7 shows the XPS spectra for the NiPPc and the Br_3^- absorbed NiPPc sample. The XPS survey spectrum (Figure S7a) shows the presence of C, N, O, and Ni elements in both samples, while Br was only detected in Br_3^- absorbed NiPPc. The appearance and enhancement of the Br peak confirms the substantial bromine absorption in NiPPc. To further examine the surface electronic structure of the absorbed bromine species, high resolution XPS of Br 3d spectra (Figure S7b) were deconvoluted into peaks at 70.1 eV, 69.1eV, and 68.1eV, corresponding to Br-Br, Br^-, and chemisorbed Br, respectively.[13, 14] The dominant peak of chemisorbed bromine indeed demonstrates the strong adsorption capacity of NiPPc for Br_3^-.

Regarding the high-resolution XPS spectrum for Ni 2p (Figure 7c), after Br_3^- adsorption, the position of the Ni 2p peak remained unchanged (at 855.9 eV, corresponding to the Ni in Ni–N_4 site),[12] albeit with a discernible reduction in

intensity. The constant peak position indicates that Ni continued to exist as Ni–N_4 sites, maintaining its oxidation state unchanged after the adsorption of Br_3^-. As XPS is a typical surface analysis technique, the X-rays can penetrate deep into the sample, but only the photoelectrons emitted from a thin surface layer of the sample can escape.[15] Therefore, we infer that this is the reason accounting for the reduced Ni 2p peak after Br_3^- adsorption.

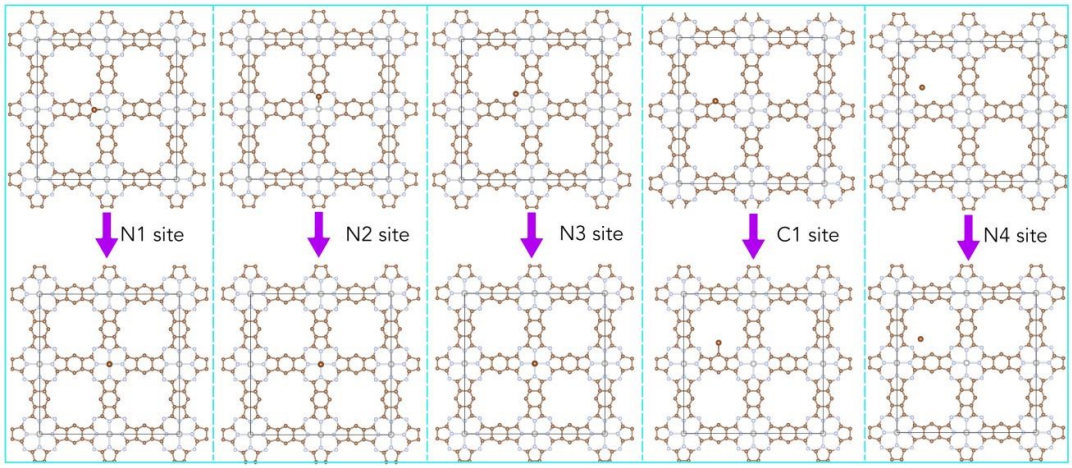

Figure S8. The optimized structure diagram of adsorption at different sites.

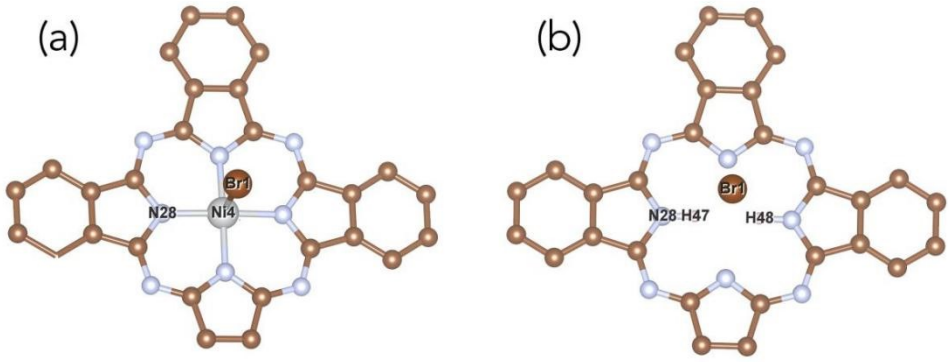

Figure S9. Structural diagram for Bader charge calculation.

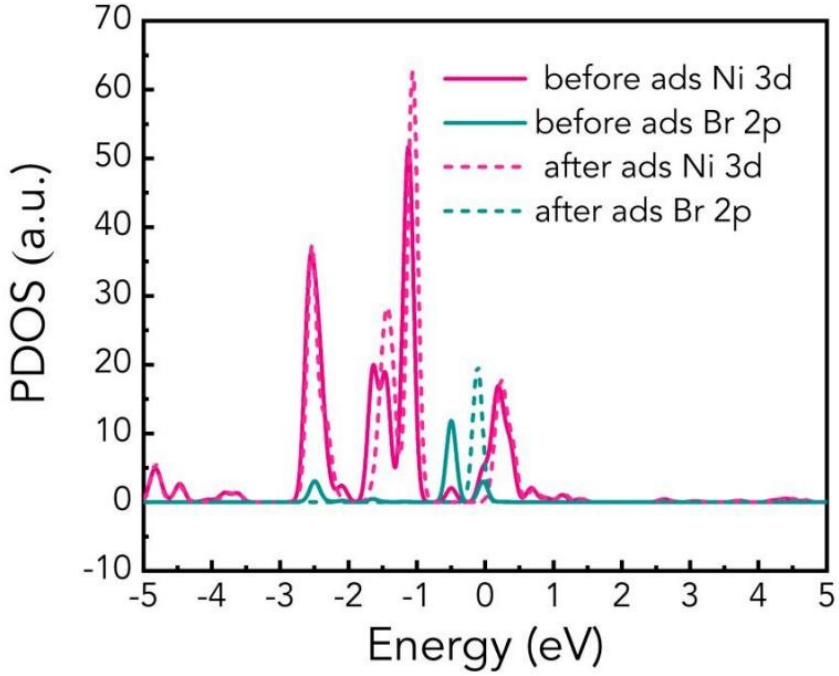

Figure S10. PDOS of Br atom before and after adsorption on NiPPc.

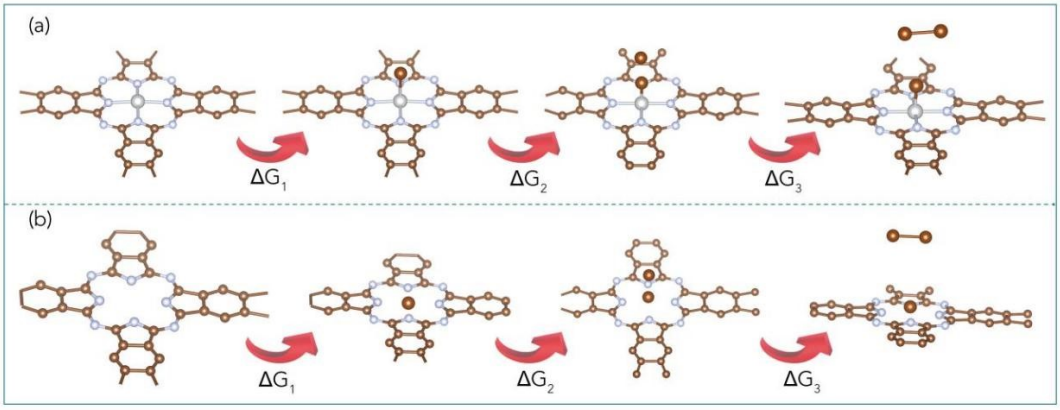

Figure S11. The structural diagrams for each step of Gibbs free energy calculation.

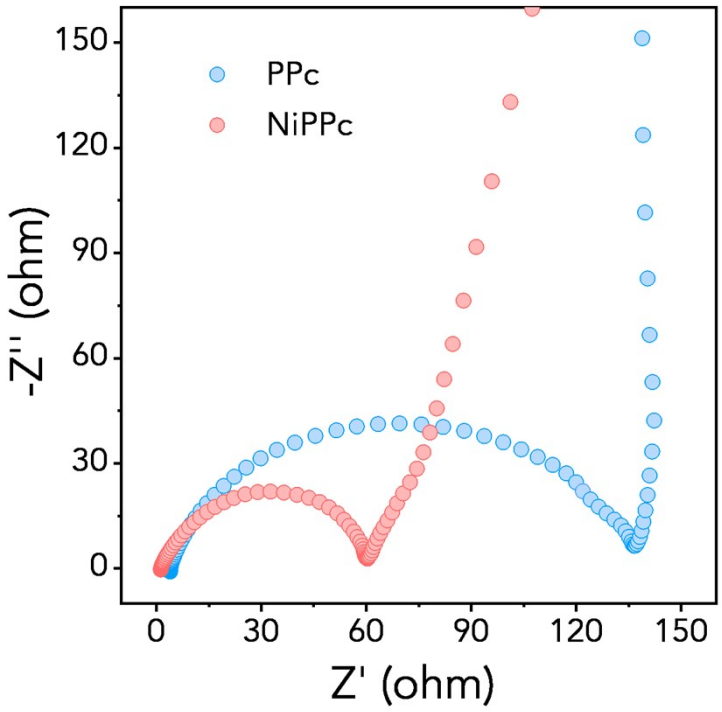

Figure S12. Electrochemical impedance spectroscopy plots of Zn||KBr-NiPPc and Zn||KBr-PPc.

Figure S13. The photographs of the zinc metal anodes from the Zn||KBr-NiPPc (left) and Zn||KBr-KB (right) cells after cycling for 24 hours at 2 A g^{-1}.

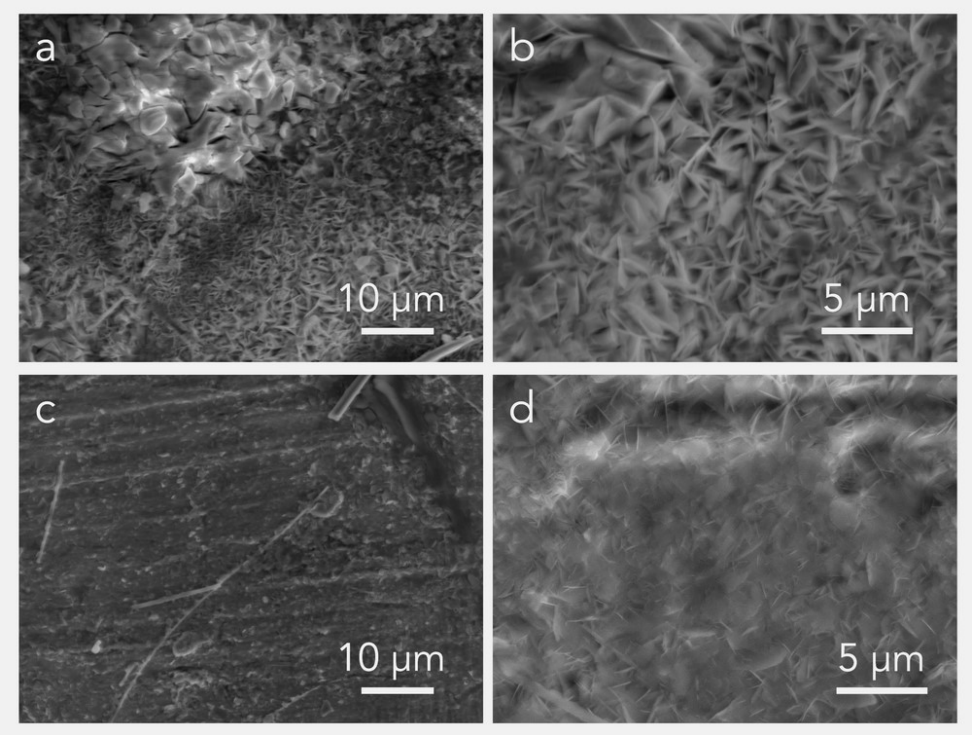

Figure S14. SEM images of zinc metal anodes from (a,b) the Zn||KBr-KB cell and (c,d) the Zn||KBr-NiPPc cell after cycling for 24 hours at 2 A g^{-1}.

To investigate the impact of bromine shuttle on the zinc anode, we have analyzed the morphologies of the zinc anodes from the Zn||KBr-NiPPc and Zn||KBr-KB cells, disassembled after 24 h of cycling. Figure S13 shows the photograph of the Zn metal anodes from Zn||KBr-NiPPc (left) and Zn||KBr-KB (right). Obviously, due to shuttle effect of bromine, the zinc anode from Zn||KBr-KB displayed a corroded, charred black appearance, with residual Br_2 (orange color) visible on the glass fiber separator. In contrast, the zinc anode from Zn||KBr-NiPPc maintained a smooth, white surface, unaffected by bromine.

Furthermore, we employed SEM for a more accurate and intuitive comparison. Figure S14a and b reveal a large number of sharp protuberances on the Zn metal anode from Zn||KBr-KB after 24 h of plating/stripping cycles, indicative of the corrosive impact of bromine. In contrast, as shown in Figure S14c and d, the zinc anode from Zn||KBr-NiPPc maintained a smooth and flat surface, which is attributed to the excellent adsorption-catalytic effect of NiPPc on bromine species.

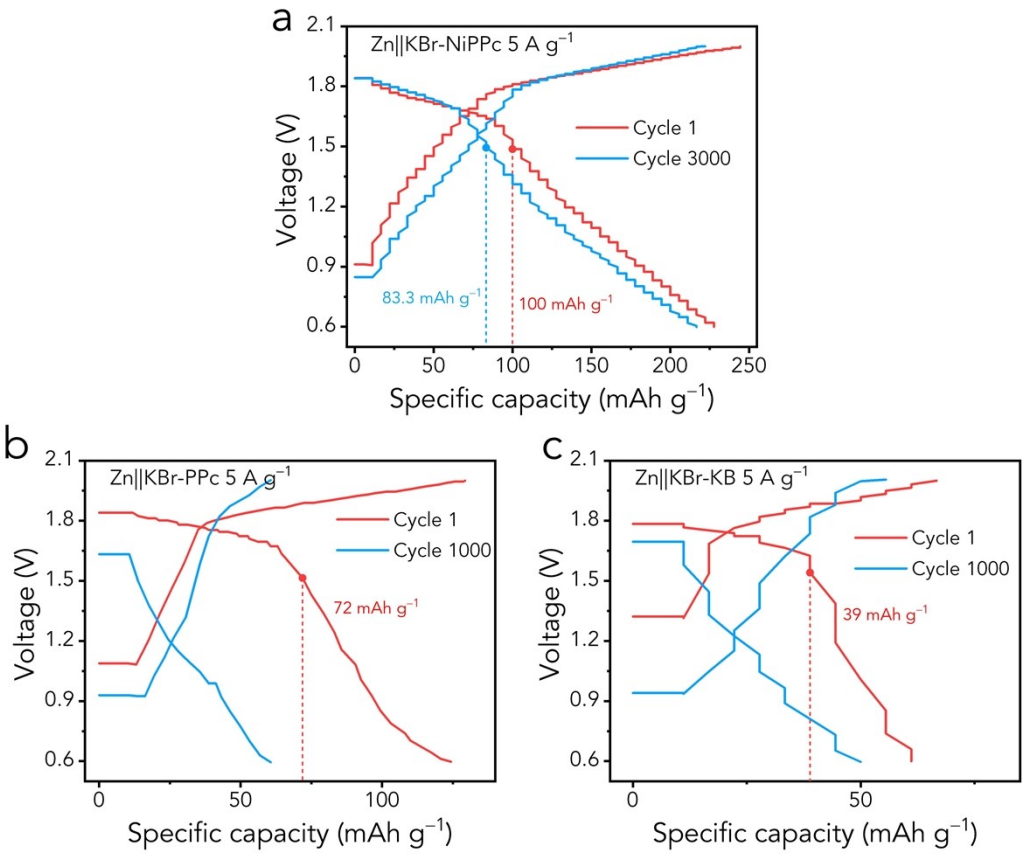

Figure S15. GCD curves of (a) the Zn||KBr-NiPPc at the 1st and 3000th cycle, (b) the Zn||KBr-PPc at the 1st and 1000th cycle, and (c) the Zn||KBr-KB at the 1st and 1000th cycle.

The charge-discharge curves of NiPPc, PPC, and KB during long cycling are shown in Figure S15. it can be observed that when using NiPPc as the cathode host, the plateau discharge specific capacity of the first cycle reached 100 mAh g^{-1}. Impressively, even after 3000 cycles, the discharge plateau still sustained a high specific capacity of 83.3 mAh g^{-1}. This indicates that the the majority of the active bromide species were well preserved after extensive cycling, validating NiPPc's superior adsorption capability for bromine species. In contrast, when using PPc as the cathode host, the plateau discharge specific capacity of the first cycle was approximately 72 mAh g^{-1}. By the 1000th cycle, no distinct discharge plateau was observed, suggesting near depletion of active Br species due to shuttle effect.

Similarly, when using KB, the discharge specific capacity of the first cycle was only 36 mAh g^{-1}, and no discernible discharge plateau can be observed by the 1000th cycle.

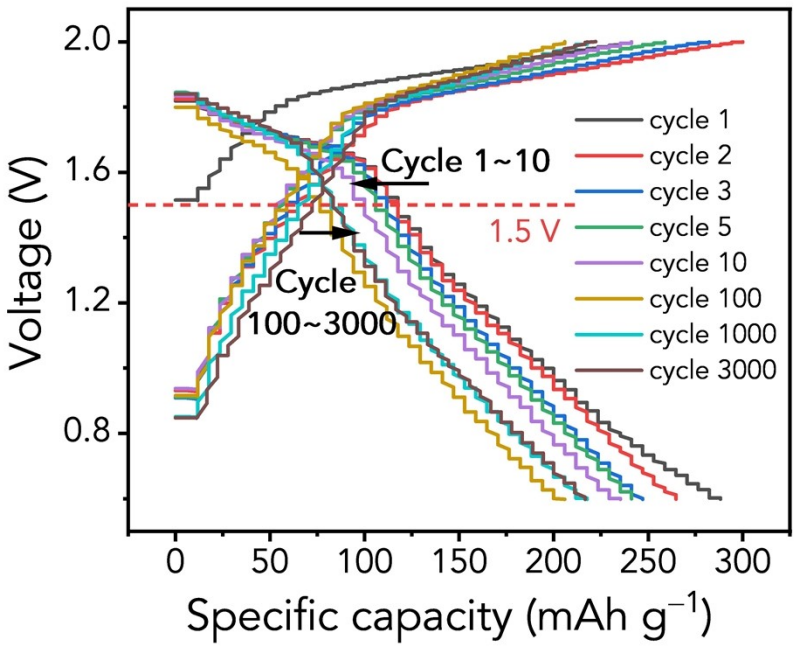

Figure S16. GCD curves of the Zn||KBr-NiPPc at the 1st, 2nd, 3rd, 5th, 10th, 100th, 1000th, and 3000th cycle.

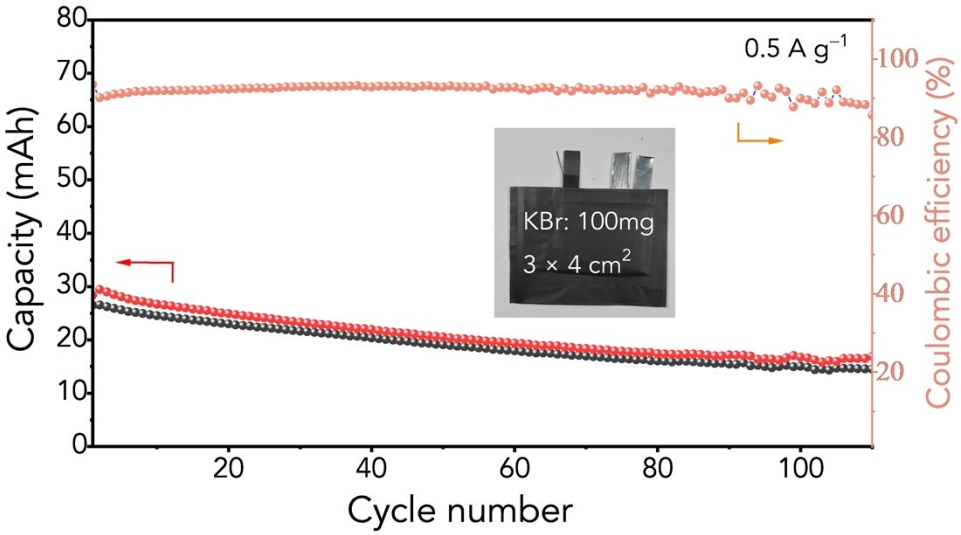

Figure S17. Cycling performance of the pouch cell using the NiPPc cathode host. Inset is the optical photo of 3 × 4 cm pouch cell.

Figure S18. Photograph of the zinc anode from the failed pouch cell after cycling.

To investigate the cause of performance decay, we disassembled the punch cell after operating for 120 cycles. As shown in Figure S18, the zinc anode had largely disintegrated into fragments or even powders, making it incapable of performing its functions as both anode and current collector, as the 0.1 mm thick zinc foil was unable to withstand such a high cycling current density of 265 mAh g^{-1}. This led to inevitable battery failure. Therefore, the key challenges in developing high-loading non-flow zinc-bromine batteries likely reside in overcoming the vulnerabilities such as the rapid consumption of zinc anode and its intense side reactions.

Table S1. The parameters for the unit cell of NiPPc with AA stacking and AB stacking.

Crystal Structure	Parameters
AA stacking	Space group: P4/mmm Lattice type: Tetragonal a (Å) = 11.0159 c (Å) = 3.1419 α= β = γ = 90°
AB stacking	Space group: I 4/mmm Lattice type: Tetragonal a (Å) = 11.0159 c (Å) = 5.18 α= β = γ = 90°

Table S2. EXAFS fitting parameters at the Ni K-edge for various samples (S_0^2=0.82)

	shell	CN	R(Å)	σ^2	ΔE_0	R factor
Ni foil	Ni–Ni	12	2.48±0.01	0.0063	7.4±0.3	0.0013
Sample	Ni–N	4.1±0.2	2.04±0.01	0.0062	-4.1±0.8	0.0035

[a]*CN*: Niordination numbers; [b]*R*: bond distance; [c]σ^2: Debye-Waller factors; [d] ΔE_0: the inner potential Nirrection. *R* factor: goodness of fit

Table S3. The adsorption energies of different sites on NiPPc.

Site	Adsorption energy (eV)
N1-3	-2.14
N4	1.23
C1	-2.11

Table S4. Comparison of Bader charge between NiPPc and PPc

Element	Bader Charge (e) (NiPPc)	Bader Charge (e) (PPc)
Br1	0.48	0.46
N28	1.11	1.23
Ni4	-0.98	
H47		-0.56

Reference

1 J. He, H. Hong, Q. Feng, X. Wang, X. Zhao, M. Xu, X. Wu, H. Li, C. Zhi and C. Han, *Chemical Engineering Journal*, 2022, **444**, 136544.

2 B. Evanko, S. J. Yoo, S.-E. Chun, X. Wang, X. Ji, S. W. Boettcher and G. D. Stucky, *Journal of the American Chemical Society*, 2016, **138**, 9373-9376.

3 G. Kresse and J. Hafner, *Physical review B*, 1993, **47**, 558.

4 G. Kresse and J. Furthmüller, *Physical review B*, 1996, **54**, 11169.

5 J. P. Perdew, K. Burke and M. Ernzerhof, *Physical review letters*, 1996, **77**, 3865.

6 L.-Y. Gan, Q. Zhang, Y. Cheng and U. Schwingenschlögl, *Physical Review B*, 2013, **88**, 235310.

7 K. Momma and F. Izumi, *Journal of applied crystallography*, 2011, **44**, 1272-1276.

8 B. Delley, *The Journal of chemical physics*, 1990, **92**, 508-517.

9 B. Delley, *The Journal of chemical physics*, 2000, **113**, 7756-7764.

10 Y. Chuminjak, S. Daothong, A. Kuntarug, D. Phokharatkul, M. Horprathum, A. Wisitsoraat, A. Tuantranont, J. Jakmunee and P. Singjai, *Electrochimica Acta*, 2017, **238**, 298-309.

11 J. Ren, M. Antonietti and T. P. Fellinger, *Advanced Energy Materials*, 2015, **5**, 1401660.

12 F. Petraki, V. Papaefthimiou and S. Kennou, *Organic Electronics*, 2007, **8**, 522-528.

13 L. G. Bulusheva, A. V. Okotrub, E. Flahaut, I. P. Asanov, P. N. Gevko, V. Koroteev, Y. V. Fedoseeva, A. Yaya and C. P. Ewels, *Chemistry of Materials*, 2012, **24**, 2708-2715.

14 L. Smykalla, P. Shukrynau, M. Korb, H. Lang and M. Hietschold, *Nanoscale*, 2015, **7**, 4234-4241.

15 J. Chastain and R. C. King Jr, *Handbook of X-ray photoelectronspectroscopy*, Perkin-Elmer Corporation, 1992, **40**, 221.